communications materials

Article

https://doi.org/10.1038/s43246-024-00624-y

Transformation of europium metal-organic framework from 3D via 2D into exfoliating 3D for enzyme immobilization

Ani Vardanyan [1] ✉, Guojun Zhou[2], Nayoung Kim[3], Tetyana M. Budnyak[4], Vadim G. Kessler [1], Insung S. Choi [3], Zhehao Huang [2] & Gulaim A. Seisenbaeva [1] ✉

Metal-organic frameworks (MOFs) have emerged as highly promising materials for hosting functional biomolecules. Here, a 1,2,4-benzenetricarboxylate ligand with a flat asymmetric shape is applied to infuse an unusual behavior to a 3D europium MOF (SLU-1). Solvent addition results in the 3D MOF splitting into a 2D one (SLU-2), and in the presence of excess water, gets cross-linked into a different 3D MOF (SLU-3) prone to spontaneous exfoliation. SLU-3 features a combination of highly hydrophilic and hydrophobic spots and serves as an attractive host for incorporating large active species. As a representative demonstration, horseradish peroxidase (HRP) is incorporated into the exfoliated 3D-layered structure by simple mixing, and secured by an outer silica layer in the form of core-shell structures. The resulting HRP-based biocatalyst exhibited enhanced stability and reusability, effectively degrading phenol. This work showcases the potential of reconfigurable MOFs, offering upheld applications through the controlled uptake and retention of biocatalytic agents.

The field of hybrid inorganic-organic porous solids is a rapidly growing and exciting area with significant potential for practical applications. Among different porous crystalline hybrid materials, metal-organic frameworks (MOFs) and porous coordination polymers have recently attracted a lot of attention[1–7]. They have a unique combination of properties, such as high surface area, chemical diversity, and unprecedented variability of pore shape/size and topology[8–10]. These properties make them promising candidates for a wide range of applications, including water treatment, water harvesting, gas storage and separation, drug delivery, sensors, and energy conversion and storage[11–14]. MOFs are a class of porous crystalline hybrid materials constructed through the coordination of metallic units called secondary building units (SBUs) and organic ligands[15–17]. The elemental structure of MOFs includes metal nodes (metal ions or metal oxide "clusters"), organic ligands, and nano-sized internal open spaces (formed spontaneously by the self-assembly of metal and ligand components). A vast majority of these structures have been based on the use of *d*-block transition metal ions together with aromatic *N*-donor ligands[18]. Lanthanide polymeric complexes, on the other hand, are less common, since these structures can be more difficult to control due to the higher coordination numbers of lanthanide ions[19]. Nonetheless, they form very intricate constructions due to their flexible coordination geometry, which attracts increasing interest from chemists, and thus many studies have been reported in the literature recently[18]. Introducing lanthanide centers into the skeleton can lead to not only distinctive architectures but also unique optical and luminescent properties derived from their *f*–*f* electronic transitions[20,21]. However, when it comes to rare-earth hybrid materials, the majority of solids found so far are coordination polymers, which contain metallic moieties that are either single polyhedra or isolated small clusters. Some 3D MOF structures have been reported using di-, tri- and tetracarboxylates[19,21,22], bipyridine[23], benzoic acid[24]. The use of benzene tri- and tetracarboxylates has the possibility to offer flat structures possessing large pores, potentially capable of incorporating large molecules, such as enzymes, and thus ensuring the maintenance of their conformation and chemical functions. Recently, special attention was drawn to possibilities to convert 3D MOFs into 2D construction by exfoliation, thus creating materials with even greater extended surface area and reactivity[25–27]. The methods for exfoliating 3D MOF into 2D MOF have been reported extensively in the previous literature[28–31]. In this paper, we report the synthesis and characterizations of three to the best of our knowledge new MOFs based on europium and 1,2,4-benzene tricarboxylate (1,2,4-BTC) revealed by continuous rotation electron diffraction (cRED) studies. One of those obtained as major product in the synthesis involving minimal amount of water was a 3D structure, which is denoted as

[1]Department of Molecular Sciences, Swedish University of Agricultural Sciences, Uppsala, Sweden. [2]Department of Materials and Environmental Chemistry, Stockholm University, Stockholm, Sweden. [3]Department of Chemistry, KAIST, Daejeon, Korea. [4]Division of Nanotechnology and Functional Materials, Department of Materials Science and Engineering, the Ångström Laboratory, Uppsala University, Uppsala, Sweden. ✉e-mail: ani.vardanyan@slu.se; gulaim.seisenbaeva@slu.se

SLU-1. In the excess of solvent, the 3D structure transformed into a new, open 2D structure (SLU-2) demonstrated structurally as dimethylformamide (DMF) solvate instead of the water-terminated one. Upon exposure to aqueous media, the layers of the 2D structure re-assembled and formed a new spontaneously exfoliating 3D structure (SLU-3). The latter was water-stable, as identified by X-ray powder study (PXRD), and was utilized in enzyme immobilization for successful removal of phenol from polluted waters.

Results and discussion

Synthetic strategy

Aiming at creation of MOF with facile transformation into a layered material, we proposed to use a flat asymmetric ligand, 1,2,4-benzene-tricarboxylic acid (1,2,4-BTC) in combination with large and highly charged, and thus not strongly polarizing, rare earth Europium cations. Flat ligands were expected to facilitate formation of layers in the structure, while their asymmetric structure was expected to make possible transformations easier. Combination of large highly charged cations with relatively large hydrophobic ligands was giving a promise of enhanced affinity towards enzyme molecules like horseradish peroxidase (HRP), known for its patchy surface[32].

The proposed strategy turned fully successful—the initially produced 3D MOF SLU-1 with uniform net of metal-ligand bonds was spontaneously transforming into a 2D structure terminated by coordinated DMF solvent molecules. In water, however, the transformation went further with re-assembly of the 2D layers into a new weakly bonded 3D structure (SLU-3) that spontaneously exfoliated into a few-layer sheets. The latter were as promised possessing high affinity to HRP and were thus used for its immobilization leading to a highly promising biocatalyst.

Structural determination

SLU-1 was produced through hydrothermal route using 1,2,4-BTC as a ligand, $Eu(NO_3)_3 \times 5H_2O$ as a metal ion precursor and acetic acid as a modulator in DMF as solvent. The material was isolated as a white crystalline powder and characterized thoroughly for its structure and morphology. The SEM and AFM images showed that SLU-1 consisted of fusiform microcrystals with a length and diameter of about 3.5 and 1.5 μm, respectively (Fig. 1A). At closer magnification, it was possible to observe layered structure on some of the crystals (Fig. 1A, B).

3DED study of the pristine products revealed the presence of two different phases (Fig. 2 and Tables S1, S2, S4, S5). The major product was a 3D SLU-1 material ($Eu(C_9H_3O_6)H_2O$) (Fig. 2E). According to FTIR and TGA (Supplementary Fig. S8) it contained interstitial DMF molecules in the pores of its structure. We observed also in addition to the major phase the plate-like crystals (Fig. 2J) resulting from the transformation of SLU-1 to the 2D SLU-2 ($Eu(C_9H_3O_6)(C_3H_7NO)$). We supposed that its formation was caused by local excess of the solvents, DMF (major) and, most importantly, water (minor), both present in the synthetic medium for SLU-1. The SLU-2 material was proved to contain DMF as bound solvent, where DMF molecules coordinated to the europium centers, altering their coordination environment and facilitating the planar arrangement of the 1,2,4-BTC ligands into layers. To test the effect of water, we have treated SLU-1 MOF with water by mixing it overnight on an orbital shaker. The samples were later collected by centrifugation and dried under nitrogen atmosphere. 3DED studies and SEM images confirmed our hypothesis, revealing a new phase (denoted SLU-3, $[Eu(C_9H_3O_6)(H_2O)_3]\cdot H_2O$) (Figs. 1C,D, S3,6, Tables S3–5), which was a result of hydration of SLU-1. When SLU-2 was subsequently exposed to water as the main solvent, the transformation proceeded further with the re-assembly of the 2D layers into above-mentioned, weakly bonded 3D structure (SLU-3). In this step, water molecules replaced the DMF in the coordination sphere of the europium ions, leading to the reformation of a 3D network that was prone to spontaneous exfoliation into few-layer sheets. The transformation from SLU-2 to SLU-3 was further confirmed by 3DED, PXRD and FTIR analyses. 3DED analysis revealed that the 3D SLU-1 MOF was built up from a net of eight-coordinated Europium cations, linked by the benzene tri-carboxylate groups. Oxygen atoms from the carboxylates ensured the completion of the coordination of the rare-earth atoms. The function of each carboxylate exhibited a different mode of connection to the rare-earth (Fig. 2E); two of them coordinated with two different rare-earths (C(12) and O(6), O(1) and C(8) with O(5) and O(8)), while the third one bridged two and chelating one europium ions (C(7), O(7), O(4)). The connection of these chains via the carboxylate ions created interconnected tunnels in the three directions with several C-C distances calculated to be between 16–18 Å, with no sufficient porosity for the encapsulation of large molecules.

Different modes of connection were noticed in the plate-like SLU-2 MOF compared with the SLU-1 3D structure. In SLU-2, one carboxylate group bridged two and chelated one europium ion (C(2), O(7) and O(1)), the second one coordinated with two different europium ions (C(11) with O(6) and O(2)), and the third bridged two lanthanide ions together (C(10) with O(5)) (Fig. 2J).

When comparing the structures of SLU-2 and SLU-3, we can observe a new mode, where the DMF molecules are washed away and the carboxylate groups of the organic linker bridged europium ions across *a* axis of SLU-2 becoming the *b*-axis in the new 3D network of SLU-3 (vertical direction in Figs. 3C, 4). In the case of SLU-2, we observed that DMF coordinated with the europium ion through the oxygen atom, whereas SLU-1 did not reveal the presence of DMF in the complex structure (Figs. 2E, J, 3A, B).

However, the FTIR analysis of SLU-1 displayed distinct peaks at 1666 cm^{-1} and 2930 cm^{-1}, corresponding to the stretching vibrations of C=O and C-H of DMF, respectively[33](Supplementary Fig. S7). Based on the results, we thought that DMF was entrapped disorderly in SLU-1 during synthesis, which was not washed away. We further compared the FTIR spectra of SLU-1 and SLU-3, which showed broader and more intensive peak at 3500 cm^{-1} from water -OH stretching vibrations; however, the peaks at 2930 cm^{-1} and 1666 cm^{-1} have disappeared as a result of water molecules replacing DMF while acting as a catalyst in the transformation to a new 3D structure.

Furthermore, the infrared spectra of both SLU-1 and SLU-3 MOFs exhibited characteristic vibration bands associated with the coordinating carboxylate functions of the ligand, found around 1550 cm^{-1} (C=O) and 1390 cm^{-1} (O-H bending)[21,34,35] (Supplementary Fig. S7).

Gas adsorption properties

The nitrogen adsorption/desorption isotherms for SLU-1 and SLU-3 MOFs are presented in Supplementary Fig. S8a. The shape of the isotherms corresponds to the characteristic Type II isotherm with the H3 type of hysteresis loop. This type of hysteresis is common for aggregates of plate-like particles, which give rise to slit-shaped pores[36]. Brunauer–Emmett–Teller specific surface area (S_{BET}) was found to be 70.5 m^2/g for the SLU-3 MOF sample. The results for SLU-1 showed a decrease in the BET surface area from 70 to 28 m^2/g, which could be a result of structural changes that follow the 3D network formation.

The non-porous structure of the MOF samples was confirmed by pore size distribution plots presented in Supplementary Fig. S8b. The peak at ca. 4 nm could be explained by the Tensile Strength Effect, which appears in the case of lamellar materials or when the material presents a fraction of large pores, with a very small neck. This is confirmed by the tendency of the isotherms to increase the volume at very high pressures (above p/p_0 9.0) (Supplementary Fig. S8a). Nitrogen isotherms cannot probe these large pores or spaces between layers. For nitrogen isotherms, the hysteresis exists only till relative p/p_0 pressure 0.45, i.e., there is no hysteresis from this point below. Therefore, the gas "trapped' in those large pores/spaces is completely released at this relative pressure p/p_0 0.45. This feature results in false peaks at 3.5–3.8 nm, which should not be considered as mesopores[37,38].

The total pore volume was found to be 0.071 cm^3/g for SLU-1 and 0.154 cm^3/g for SLU-3. The detected desorption average pore diameter for SLU-1 was 10.2 nm, and for SLU-3, 8.7 nm.

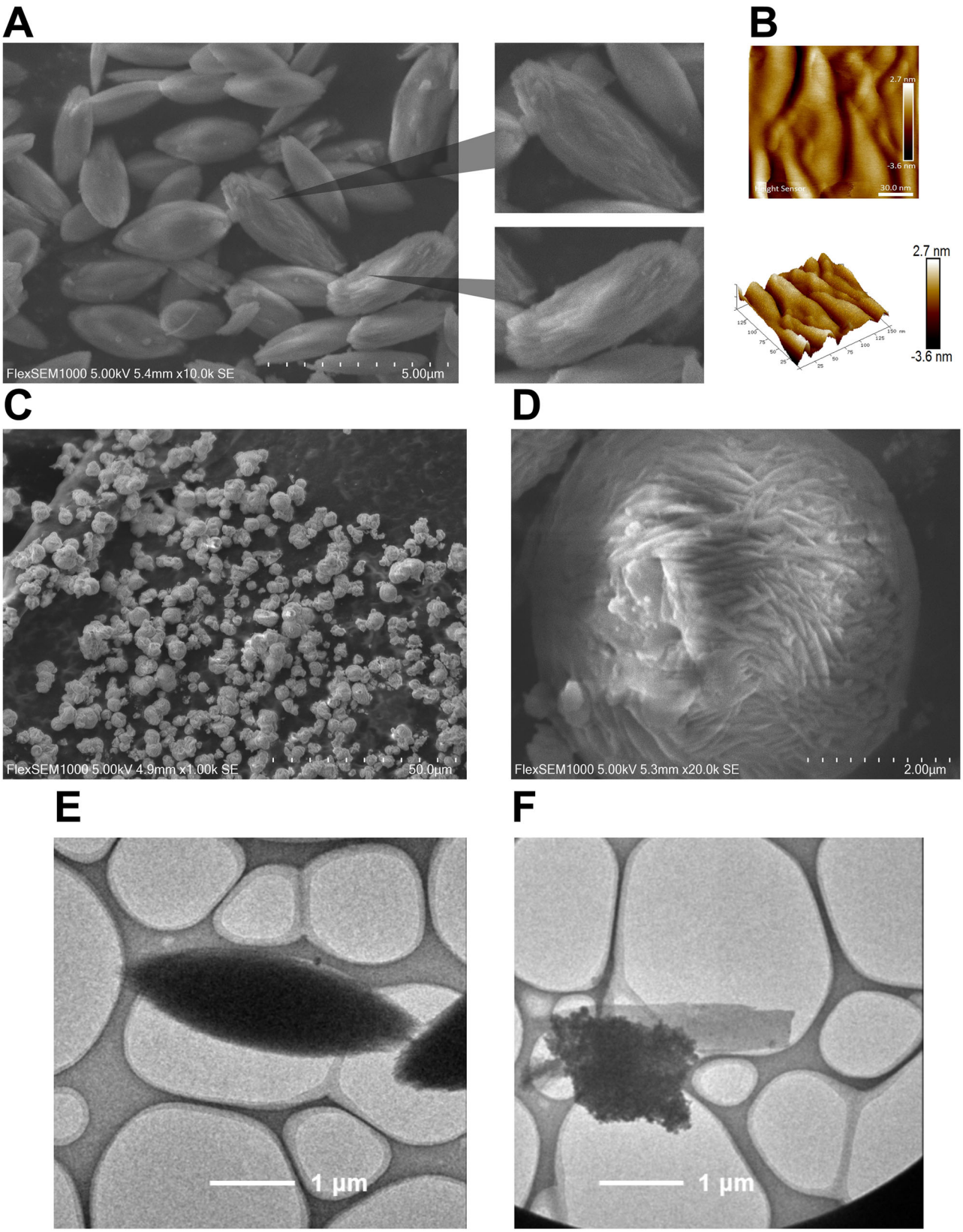

Fig. 1 | SEM, AFM and TEM images of the three dimensional SLU-1 and SLU-3 MOFs. SEM image of 3D SLU-1 (**A**), AFM image of 3D SLU-1 (**B**), SEM images of SLU-3 after treating SLU-1 with water (**C**, **D**), TEM images of 3D MOF SLU-1 (**E**) and 2D MOF SLU-2 (**F**).

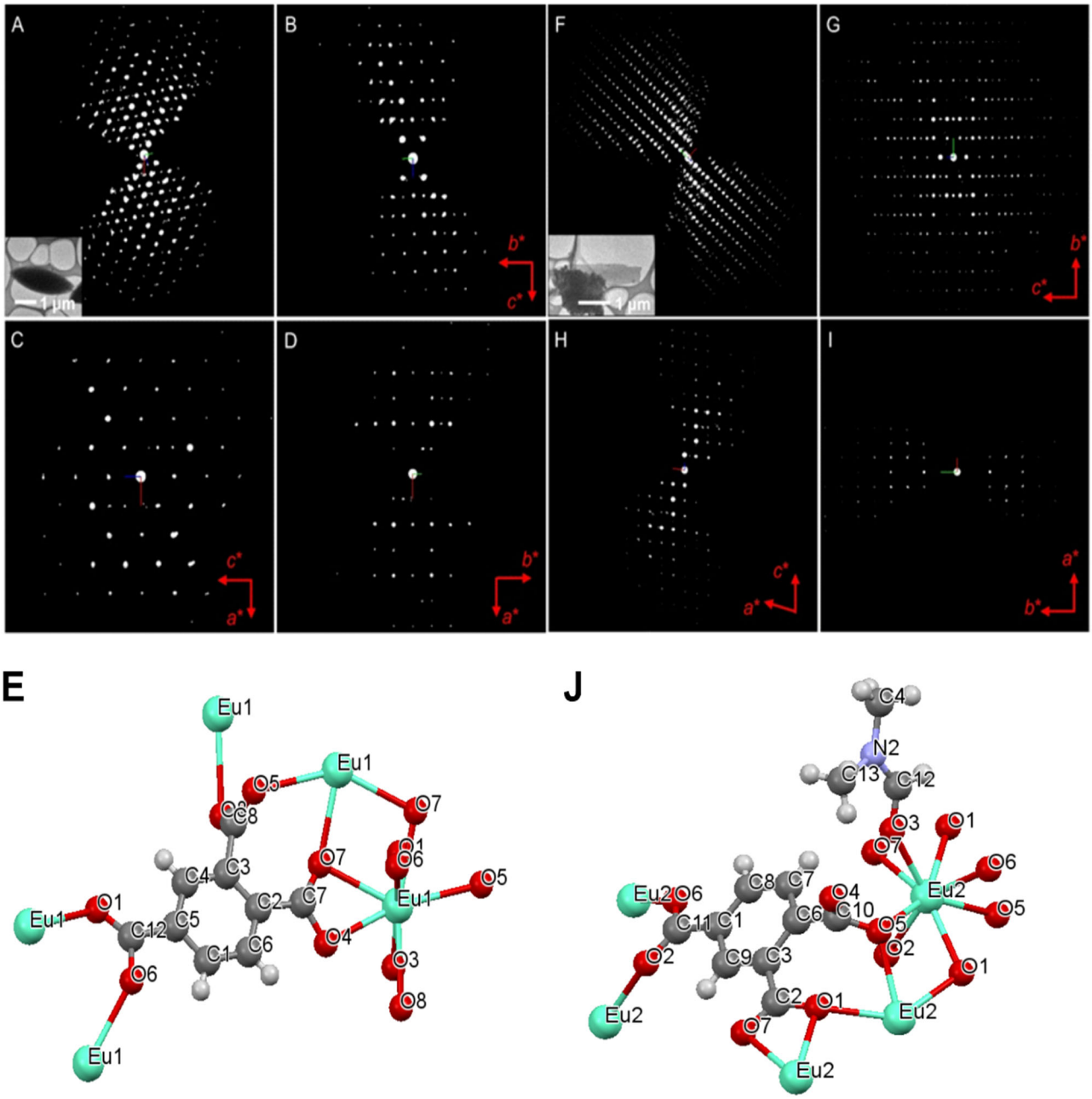

Fig. 2 | Structural analysis of SLU-1 and SLU-2 by 3DED. The reconstructed 3D reciprocal lattices for SLU-1 (**A**) and SLU-2 (**F**). Inset: TEM image of the crystal, from which the cRED data were collected. 2D slices from the reconstructed 3D reciprocal lattice showing the 0*kl* plane for SLU-1 (**B**), SLU-2 (**G**); *h*0*l* plan for SLU-1 (**C**), SLU-2 (**H**); *hk*0 plan for SLU-1 (**D**), SLU-2 (**I**). Ball and stick view of the connection mode of 1,2,4-BTC in SLU-1 (**E**) and SLU-2 (**J**).

Stability of synthesized MOFs

Due to the relatively weak metal coordination bonds, some MOFs have poor chemical and thermal stability and are very sensitive to water[39]. Herein, the thermal stability of SLU-1 and SLU-3 was characterized by thermogravimetric analyses, which were performed under O_2 gas flow (Supplementary Fig. S9). From Supplementary Fig. S9 it could be concluded that both compounds remained unchanged to 100 °C loosing then free water molecules, residual ethanol and DMF trapped in the pores. Partial decomposition with presumably some structural changes occurred in the interval 100–320 °C with a stage of complete decomposition starting from 450 °C and finishing at 500 °C. Finally, the residual carbon is burnt out in the temperature interval 500–700 °C.

To further explore the stability of SLU-3 MOFs, we conducted additional experiments by exposing the MOFs to aqueous solutions with pH levels ranging from 3 to 8, which are compatible with enzyme activity. PXRD analysis was performed to monitor any structural changes. The results (Supplementary Fig. S10) showed that the SLU-3 MOFs maintained their structural integrity across all tested pH levels, indicating excellent stability. Additionally, an increase in crystallinity was observed when the pH was either increased or decreased from the neutral pH used during synthesis, suggesting that the MOF structure can adapt to different pH environments without losing its crystalline nature.

Enzyme immobilization

Enzyme encapsulation and immobilization have been increasingly studied for the last years, using MOFs as supports[40–44]. These highly porous and crystalline materials have demonstrated excellent potential in enhancing enzyme stability, activity, and recyclability[45]. Here we tested two methods for

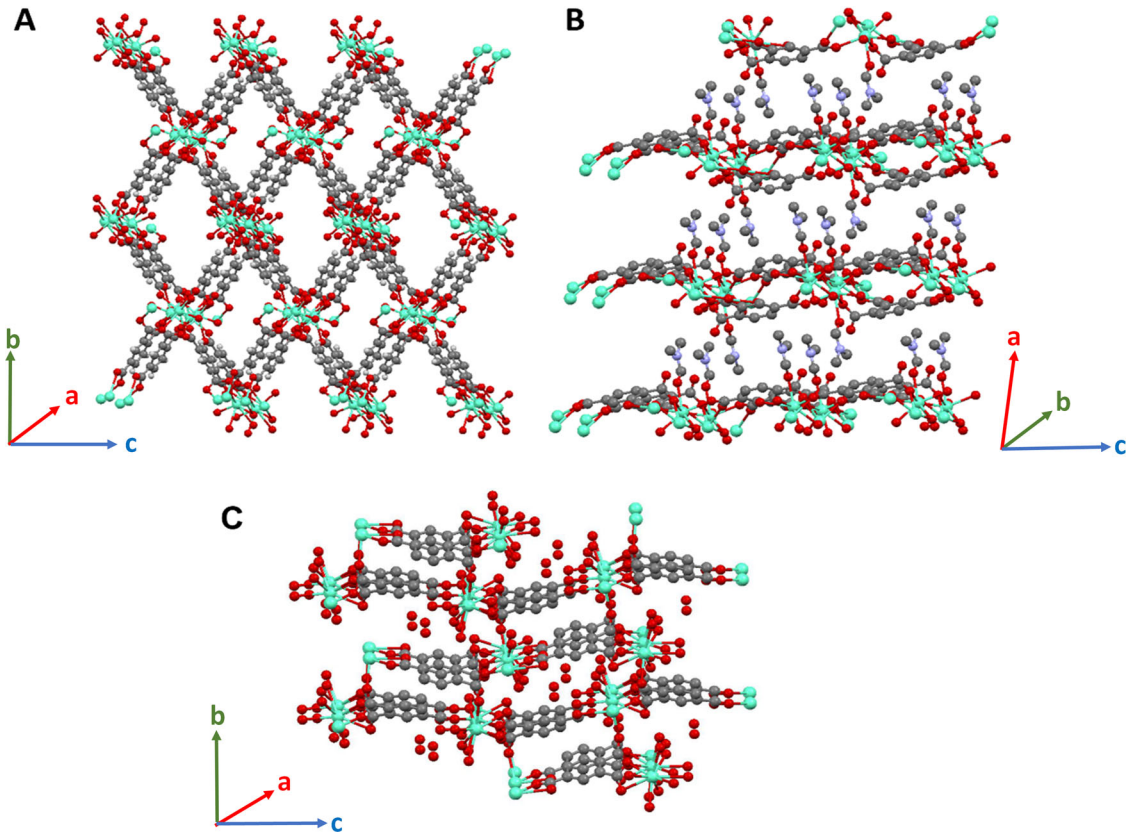

Fig. 3 | Ball and stick views of the obtained structures. 3D SLU-1 (**A**), 2D SLU-2 (**B**) and new 3D SLU-3 MOF (hydrated form) (**C**) structures along the *b* and *a* axes respectively. Europium and carbon atoms from the organic ligand are turquois and grey respectively.

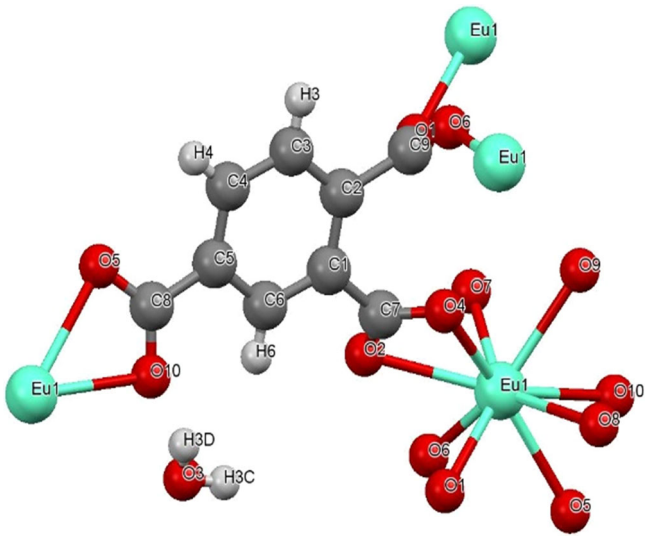

Fig. 4 | Ball and stick view of the connection mode of 1,2,4-BTC in SLU-3.

HRP immobilization: adsorption and core–shell immobilization. In the case of core-shell immobilization, the adsorbed enzyme was further covered by silica layer, achieved through Sol-Gel chemistry. Immobilization was confirmed through AFM topographic imaging, along with direct concentration and activity measurements. Figure 5 shows the aggregation of the enzyme on the layers as well as between the layers of SLU-3 MOF. Similar aggregations were previously noticed in the AFM images of native HRP enzyme[46].

Both Bradford assay and enzyme activity assay showed similar results in the amount of immobilized enzyme, reaching up to 1.8 U/mg. To compare the two synthesized biocatalysts (HRP-MOF and CS-HRP-MOF) we performed a standard 2,2′-azino-bis(3-ethylbenzothiazoline-6-sulfonic acid) diammonium salt (ABTS) oxidation tests for several consecutive cycles until the relative activity was below 80%. As shown in Fig. 6A, both biocatalysts showed high reusability potential by keeping the enzyme activity high. However, CS-HRP-MOF could be recycled for at least 4 times and still retained more than 70% of its original activity, suggesting that the core-shell structure on HRP-MOF had robust operation stability.

In comparison, the adsorbed HRP-MOF lost more than 60% of its activity after 3 cycles. This result may be due to the fact that silica layer around the MOF frame reduces enzyme leaching and improves the enzyme stability. Similar effect was noticed by Cui et al. where the Catalase enzyme encapsulated in ZIF-8 MOF showed better stability after covering with silica layer[8]. To test this hypothesis, leaching experiments were conducted with both samples in several cycles. Supplementary Fig. S11 shows the difference in leaching percentage between CS-HRP-MOF and HRP-MOF. It was clear that without the silica layer, the amount of desorbed enzyme was several times higher, however, enzyme activity decreased after four cycles for both MOF samples. Similar results were reported in a study by Wang et al. in 2019, where HRP was immobilized into ZIF-8 MOF via biomineralization and surface adsorption[47]. They achieved high adsorption and overall immobilization yield, providing good reusability over several cycles, maintaining the relative activity at about 80% for the first four cycles. The activity then decreased due to continuous enzyme leakage (up to 30%), caused by partial destruction of the framework. This may be attributed to the enzyme media used for the experiments. In fact, it has been previously reported that many MOF structures are not stable in various buffer solutions, including phosphate buffer[48–50]. To study this phenomenon with the new MOF structures, we repeated the experiments by replacing phosphate buffer with Milli-Q water. The reusability of the MOF improved greatly, confirming the theory of framework destruction by the buffer solution. Figure 6B depicts the ABTS oxidation test, which was conducted over 11 cycles within 40 days at room temperature. For the first 8 cycles, both

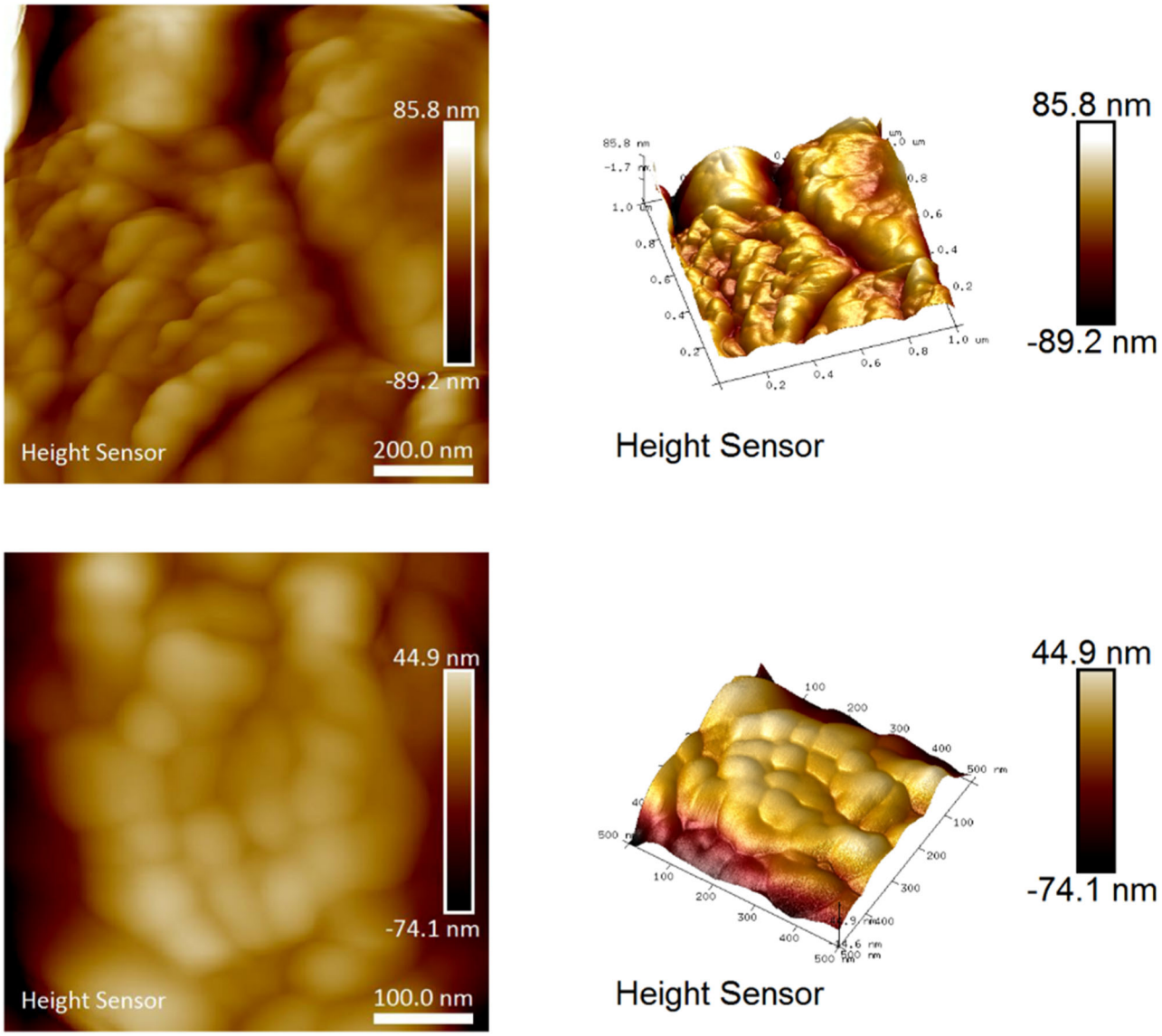

Fig. 5 | AFM images of HRP immobilized SLU-3 MOF at different magnifications.

Fig. 6 | Reusability of HRP-MOF compared to silica covered CS-HRP-MOF. Buffer conditions (**A**), in water (**B**). The error bars are the standard deviation of the data set.

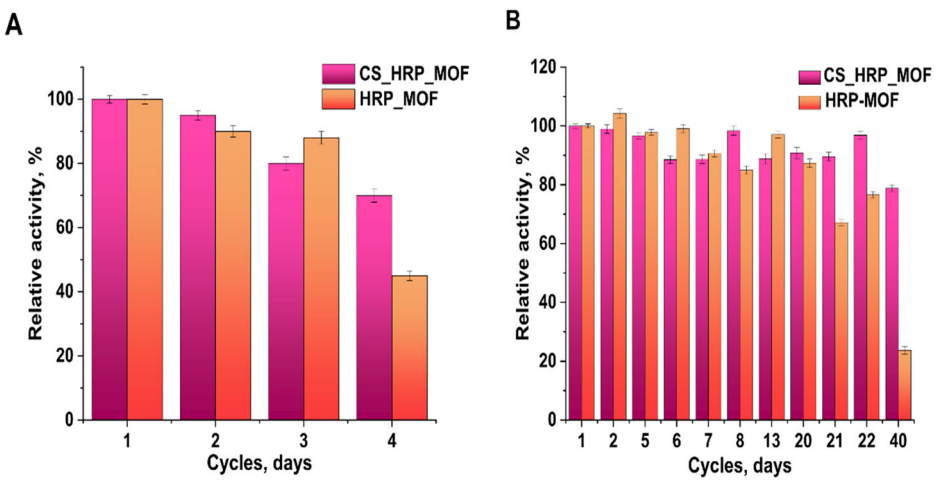

biocatalysts (HRP-MOF and CS-HRP-MOF) maintained residual activity above 80%. However, the silica layer significantly enhanced the stability of the CS-HRP-MOF sample, sustaining high activity even after 40 days.

Phenol degradation

Due to its high specificity, mild reaction conditions and environmentally friendliness, immobilized enzymes have been widely applied for organic pollutants degradation in aqueous environment[46,51–56]. To assess the potential application of CS-HRP-MOF in simulated wastewater, phenol was employed as a target organic contaminant. The degradation efficiency was determined by UV–VIS measurement and the calibration curve is displayed in supplementary materials (Supplementary Fig. S12).

The results depicted in Fig. 7 shows that CS-HRP-MOF was highly effective in the treatment of phenol at concentration of 20 µg/mL. In the first 15 min of the reaction, yellow shade colored degradation product was detected with a peak at 399 nm. After 5 h of reaction, the peak at 399 nm disappeared while the peak at 299 nm decreased as well. Similar reaction was observed previously by Elena-Florentina Grosu 2018, where same peaks were established by free HRP and peroxidase/layered double hydroxide catalysts[57]. The yellow colored intermediates are a result of polymerization of phenol at the beginning of the reaction, which disappears after several hours suggesting that the enzyme continues the oxidation of both phenol and polyphenol. According to UV–VIS measurements more than 80% of phenol was removed by immobilized HRP-MOF complex. In order to compare the results of present study with similar works, the corresponding data were collected as presented in Table S6. Considering the low biocatalyst dosages used in this study, we could conclude that the new CS-HRP-MOF shows comparable if not better efficiency for phenol removal.

Conclusions

We report the synthesis and structural determination of new lanthanide MOFs, built up from edge-sharing rare-earth polyhedra linked by benzene tricarboxylate ligands. The 3D-MOF was transforming on contact with water to a new two-dimensional plate like structure, which eventually transitioned to a new 3D network. The construction of all hydrated, dehydrated and intermediate forms has been determined by cRED method, showing changes in the coordination mode of rare earth and in the connection mode of the carboxylate. The synthesized MOF was then tested for enzyme immobilization by adsorption and core-shell structure formation. The further study revealed good adsorption characteristics of up to 1.8 U/mg, which contributed to high phenol degradation activity of the biocatalyst. The CS-HRP-MOF composite was able to degrade more than 80% of phenol at high initial concentration of 20 µg/mL, making the synthesized MOF a promising support material for enzyme immobilization.

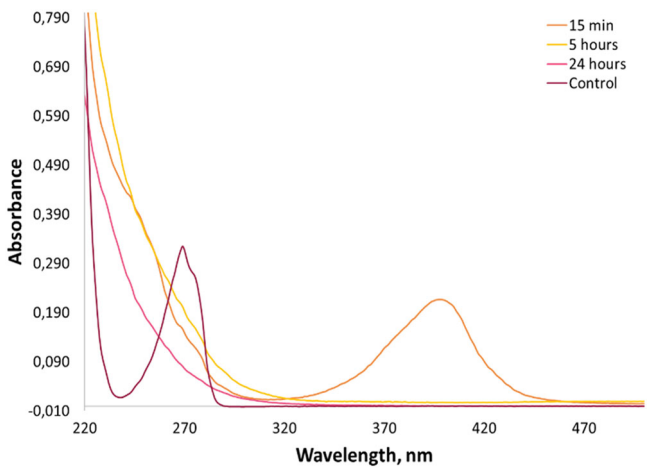

Fig. 7 | Enzymatic degradation of phenol by CS-HRP-MOF complex followed by UV–VIS measurements.

Materials and methods

Chemicals

All the chemicals were obtained commercially and used without further purification. $Eu(NO_3)_3 x5H_2O$ (CAS No: 100587-95-9), 1,2,4-benzene tricarboxylic acid (CAS No: 528-44-9), dimethyl formamide (DMF) (CAS No: 68-12-2), acetic acid (CAS No: 64-19-7), horseradish peroxidase (CAS No: 9003-99-0), 2,2′-azino-bis(3-ethylbenzothiazoline-6-sulfonic acid) diammonium salt (ABTS) (CAS No: 30931-67-0) Phenol (CAS No: 108-95-2), tetraethyl orthosilicate (TEOS) (CAS No: 78-10-4) and ammonium fluoride (NH_4F) (CAS No: 12125-01-8) were purchased from Sigma Aldrich.

Synthesis

SLU-1 MOF was synthesized via solvothermal route. Typically, 1,2,4-BTC (0.105 g) was dissolved in 23.5 mL of N,N-Dimethylformamide (DMF). To this solution $Eu(NO_3)_3$ x $5H_2O$ (0.214 g) was added and placed on a shaker for 10 min to react with the ligand. After forming a clear solution, 1.5 mL dry acetic acid was added as an acid modulator. The mixture was sealed in a 125 mL Teflon-lined steel autoclave and heated to 130 °C for 96 h under autogenous pressure. The resulting solution was then filtered and white crystallites were collected, washed 4 times with ethanol and dried under nitrogen atmosphere. SLU-2 was discovered originally as minor admixture to SLU-1 in the crude product of the synthesis. Treatment of SLU-1 in aqueous media appears to transform it into the 2D network which eventually forms a new 3D structure SLU-3 according to powder XRD data.

Characterization

PXRD patterns were collected with a Bruker D8 Quest ECO diffractometer having a Photon-III area detector and using MoKα radiation ($\lambda = 0.71073$ Å). Fourier Transform Infrared (FTIR) analyses were performed on a Perkin Elmer Spectrum 100 FT-IR Spectrometer using KBr pellets. Thermogravimetric analyses (TGA) were achieved using Perkin Elmer Pyris 1 TGA, with a heating rate of 5 °C min^{-1} under air flow. Atomic Force Microscope (AFM) images were taken with a Bruker Dimension FastScan instrument using a FastScan-B probe with a nominal tip radius of 5 nm and a scan rate of 1–3 Hz. Nanoscope analysis software was used for data processing. Nitrogen adsorption/desorption isotherms were measured at −196 °C with Micromeritics ASAP 2020 Surface Area and Porosity analyzer. The samples were previously degassed at 130 °C under high vacuum for at least 8 h. Specific surface area was estimated by BET method and external/micropore surface area by t-plot method.

Structure determination

The three-dimensional electron diffraction (3DED) studies were performed on a JEOL JEM2100 microscope operating at 200 kV (Cs 1.0 mm, point resolution 0.23 nm). Transmission electron microscopy (TEM) images were recorded on a Gatan Orius 833 CCD camera (resolution 2048 × 2048 pixels, pixel size 7.4 µm). Electron diffraction patterns were collected with a Timepix pixel detector QTPX-262k (512 × 512 pixels, pixel size 55 µm, Amsterdam Sci. Ins.). The cRED data were acquired using the software *Instamatic*[58]. The tilting rate was set at 0.45 s^{-1}, and with an exposure time of 0.3 s. To minimize beam damage and maximize data quality, each data set was collected within 4 min[59]. The data sets were processed using XDS[60], and structure determination was conducted using SHELX package[61,62].

Pawley fitting was conducted with software TOPAS Academic (IV) for refining the unit cell parameters (Supplementary Figs. S1–3). The background was fitted with 16th order Chebychev polynomial. The refinement was conducted using a Pearson VII type peak profile function, followed by the refinement of unit cells and zero-shift. The unit cell parameters were refined to $a = 8.464(1)$ Å, $b = 18.223(9)$ Å, $c = 11.976(2)$ Å, and $\beta = 91.5(1)°$ for SLU-1, $a = 11.116(7)$ Å, $b = 7.828(5)$ Å, $c = 19.891(22)$ Å, and $\beta = 98.27(4)°$ for SLU-2 and $a = 6.0944(2)$ Å, $b = 9.6132(3)$ Å, and $c = 20.0277(9)$ Å for SLU-3. The *R*-values were converged to $R_p = 5.9\%$, $R_{wp} = 8.8\%$, $R_{exp} = 4.4\%$ for SLU-1, $R_p = 5.5\%$, $R_{wp} = 7.0\%$, $R_{exp} = 5.6\%$ for SLU-2 and $R_p = 2.9\%$, $R_{wp} = 3.8\%$, $R_{exp} = 2.9\%$ for SLU-3. To further validate the structures, the (PXRD) patterns were calculated by using the

structural model obtained from (cRED) analysis, and which agreed well with the observed PXRD patterns (Supplementary Figs. S4–6).

Enzyme immobilization

HRP enzyme was immobilized by two different methods: physical adsorption and the adsorption followed by core shell structure formation. For physical adsorption (denoted HRP-MOF), 100 mg MOF was mixed with 10 mL solution of HRP in phosphate buffer (pH = 7) and concentration of 20 U/mL. After placing the mixture on an orbital shaker overnight, the particles were collected by centrifugation and washed with phosphate buffer to get rid of unattached enzyme molecules. The amount of adsorbed enzyme was determined by Bradford assay and by measuring the residual enzyme activity in the supernatant.

For core-shell structure (denoted CS-HRP-MOF), the MOF was first separated from the enzyme solution by centrifugation and 5 mL ethanol, 5 mL water was added afterwards. To this solution 200 µl NH_4F and 4 mL TEOS was added slowly to form the silica layer. The mixture was put on a shaker and mixed until the gel formation (~5 h). The gel was later washed out with ethanol and water 3 times and the immobilized enzyme was freeze dried overnight. The amount of immobilized enzyme was determined by Bradford and enzyme activity assays measured before and after enzyme immobilization (enzyme concentration was also measured in the supernatant after the gel wash).

Bradford assay

For Bradford assay protein standards were prepared in the same buffer as the HRP by diluting bovine serum albumin (BSA) protein with final concentrations ranging between 0.1 and 1.4 mg/mL. All the standards and the unknown HRP sample with a volume of 0.1 mL, were mixed with 3 mL Bradford reagent and left to react for 30 min. The samples were then transferred into cuvettes and measured for the absorbance at 595 nm.

Enzyme activity assay

The enzyme activity was measured through ABTS oxidation test where the rate of oxidation was monitored by UV–VIS. One unit of enzyme activity was defined as the amount of enzyme required to oxidize 1 µmol of ABTS per minute per unit volume and is expressed in U/mL. Triplicate measurements were performed for each assay of enzyme activity. ABTS was prepared in sodium phosphate buffer (pH = 7) and a final concentration of 0.2 mM. For activity assay with peroxidase enzyme, 3 µL of 3.6% hydrogen peroxide (H_2O_2) was added to activate the enzyme.

To determine the core shell immobilized enzyme activity, 100 mg HRP-MOF samples were placed in 10 mL ABTS solution (0.2 mM) and 30 µL of 3.6% H_2O_2 was added to start the oxidation reaction. As soon as the dye started changing the color, small aliquots from ABTS solution were taken every set time of intervals, filtered with syringe filters and measured for their absorption at 420 nm by UV–VIS. For each cycle, at least 3 measurements were performed to assure linear growth of enzyme activity. After the first cycle of activity measurement, ABTS was removed by centrifugation and 10 mL sodium phosphate buffer (pH = 7) was added to the HRP-MOF sample and put on a shaker overnight to get rid of the excess ABTS in the samples.

Enzyme reusability and leaching

The reusability of immobilized HRP was assessed by performing several consecutive operating cycles using ABTS solution as the substrate. The samples (HRP-MOF and CS-HRP-MOF) were collected and washed with phosphate buffer (pH = 7) solution after each batch and then added to the next cycle, respectively. The reusability was defined as the ratio of the activity for the immobilized HRP after recycling to its initial activity.

Removal of phenol

Enzyme activity was also tested on phenol degradation by mixing 50 mg HRP-MOF sample with 20 µg/mL phenol solution. Phenol standard solutions were prepared within the concentration range of 1–50 µg/mL, and measured by UV–VIS at 293 nm. The final phenol concentration after the contact with immobilized enzyme was then calculated from the established calibration curve.

Supporting information

Pawley fitting results for SLU-1, SLU-2, and SLU-3; Simulated PXRD patterns for SLU-1, SLU-2, and SLU-3 MOFs; Continuous rotation electron diffraction (cRED) data collection details for SLU-1, SLU-2, and SLU-3 MOFs; Crystallographic data for SLU-1, SLU-2, and SLU-3; Table with Pawley fitting results for SLU-1, SLU-2 and SLU-3; FTIR of compounds SLU-1 and SLU-3; Nitrogen adsorption/desorption isotherms and pore size distribution for SLU-1 and SLU-3 MOFs; TGA analysis for SLU-1 and SLU-3 MOFs; PXRD patterns of SLU-3 MOF at different pH; HRP enzyme desorption data; Phenol calibration curve; Comparison data for phenol removal by using immobilized HRP.

Data availability

Full details of structure solution and refinement can be obtained free-of-charge from the Cambridge Crystallographic data Centre at https://www.ccdc.cam.ac.uk citing deposition numbers 2304342, 2304343, 2334881 for SLU-1, SLU-2 and SLU-3, respectively.

Received: 3 May 2024; Accepted: 26 August 2024;
Published online: 12 September 2024

References

1. Yusuf, V. F., Malek, N. I. & Kailasa, S. K. Review on metal-organic framework classification, synthetic approaches, and influencing factors: applications in energy, drug delivery, and wastewater treatment. *ACS Omega* **7**, 44507–44531 (2022).
2. Gutterød, E. S. et al. Hydrogenation of CO_2 to methanol by Pt nanoparticles encapsulated in UiO-67: deciphering the role of the metal-organic framework. *J. Am. Chem. Soc.* **142**, 999–1009 (2020).
3. Lillerud, K. P., Olsbye, U. & Tilset, M. Designing heterogeneous catalysts by incorporating enzyme-like functionalities into MOFs. *Top. Catal.* **53**, 859–868 (2010).
4. Hafizovic, J. et al. The inconsistency in adsorption properties and powder xrd data of mof-5 is rationalized by framework interpenetration and the presence of organic and inorganic species in the nanocavities. *J. Am. Chem. Soc.* **129**, 3612–3620 (2007).
5. Rowsell, J. L. C. & Yaghi, O. M. Metal-organic frameworks: a new class of porous materials. *Microporous Mesoporous Mater.* **73**, 3–14 (2004).
6. Wang, L. et al. Metal-organic frameworks for energy storage: batteries and supercapacitors. *Coord. Chem. Rev.* **307**, 361–381 (2016).
7. Mi, X., Li, X., Wang, C. C. & Wang, B. Preferential elimination of negatively charged micropollutants in water over cerium-based metal–organic frameworks. *Sep. Purif. Technol.* **326**, 124774 (2023).
8. Cui, J., Feng, Y. & Jia, S. Silica encapsulated catalase@metal-organic framework composite: a highly stable and recyclable biocatalyst. *Chem. Eng. J.* **351**, 506–514 (2018).
9. Serre, C. et al. Characterisation and luminescent properties of a new three-dimensional lanthanide trimesate: M((C_6H_3)-$(CO_2)_3$) (M = Y, Ln) or MIL-78. *J. Mater. Chem.* **14**, 1540–1543 (2004).
10. Wang, Y. et al. Two-dimensional metal-organic frameworks with unique oriented layers for oxygen reduction reaction: tailoring the activity through exposed crystal facets. *CCS Chem.* **4**, 1633–1642 (2022).
11. Jiang, S. et al. Metal-organic frameworks for breakthrough separation of 2-butene isomers with high dynamic selectivity and capacity. *Angew. Chem. Int. Ed.* **62**, e202302036 (2023).
12. Bonneau, M., Lavenn, C., Ginet, P., Otake, K. I. & Kitagawa, S. Upscale synthesis of a binary pillared layered mof for hydrocarbon gas storage and separation. *Green Chem.* **22**, 718–724 (2020).
13. Hanikel, N. et al. MOF linker extension strategy for enhanced atmospheric water harvesting. *ACS Cent. Sci.* **9**, 551–557 (2023).

14. Zheng, Z. et al. High-yield, green and scalable methods for producing MOF-303 for water harvesting from desert air. *Nat. Protoc.* **18**, 136–156 (2023).
15. Dutt, S., Kumar, A. & Singh, S. Synthesis of metal organic frameworks (MOFs) and their derived materials for energy storage applications. *Clean Technol.* **5**, 140–166 (2023).
16. Li, H., Eddaoudi, M., O'Keeffe, M. & Yaghi, O. M. Design and synthesis of an exceptionally stable and highly porous metal-organic framework. *Nature* **402**, 276–279 (1999).
17. Annamalai, J. et al. Synthesis of various dimensional metal organic frameworks (mofs) and their hybrid composites for emerging applications – a review. *Chemosphere* **298**, 134184 (2022).
18. Long, D. L., Blake, A. J., Champness, N. R. & Schröder, M. Lanthanide co-ordination frameworks of 4,4'-bipyridine-N,N'-dioxide. *Chem. Commun.* **15**, 1369–1370 (2000).
19. Cao, R. et al. Syntheses and characterizations of three-dimensional channel-like polymeric lanthanide complexes constructed by 1,2,4,5-benzenetetracarboxylic acid. *Inorg. Chem.* **41**, 2087–2094 (2002).
20. Antic-Fidancev, E., Serpaggi, F. & Férey, G. Optical study of praseodymium dicarboxylate $[Pr(H2O)]_2[O_2C(CH_2)_3CO_2]_3{\cdot}4H_2O$. *J. Alloy. Compd.* **340**, 88–94 (2002).
21. Surblé, S., Serre, C., Millange, F. & Férey, G. Structural changes upon dehydration of $Pr(III)(H_2O)\{C_6H_3(CO_2)_3\}$ or MIL-81: a new three-dimensional praseodymium 1,2,4-benzenetricarboxylate with a one dimensional inorganic sub-network. *Solid State Sci.* **8**, 413–417 (2006).
22. Reineke, T. M., Eddaoudi, M., Fehr, M., Kelley, D. & Yaghi, O. M. From condensed lanthanide coordination solids to microporous frameworks having accessible metal sites. *J. Am. Chem. Soc.* **121**, 1651–1657 (1999).
23. Long, D. et al. Lanthanum coordination networks based on unusual five-connected topologies. *J. Am. Chem. Soc.* **123**, 3401–3402 (2001).
24. Tao, Y. et al. Multi-responsive luminescent sensor based on three dimensional lanthanide metal-organic framework. *New J. Chem.* **42**, 19485–19493 (2018).
25. Wu, P. et al. Exfoliation of metal–organic frameworks to give 2D MOF nanosheets for the electrocatalytic oxygen evolution reaction. *Angew. Chem. Int. Ed.* **63**, e202402969 (2024).
26. Shao, B. et al. Oriented exfoliating 3D metal–organic frameworks into ultrathin metal–organic nanosheets with different crystal faces. *Adv. Func. Mater.* **34**, 2315911 (2024).
27. Feng, L., Wang, K. Y., Day, G. S., Ryder, M. R. & Zhou, H. C. Destruction of metal–organic frameworks: positive and negative aspects of stability and lability. *Chem. Rev.* **120**, 13087–13133 (2020).
28. Pang, W. et al. Exfoliation of metal–organic frameworks into efficient single-layer metal–organic nanosheet electrocatalysts by the synergistic action of host–guest interactions and sonication. *Nanoscale* **12**, 3623–3629 (2020).
29. Huang, J. et al. Electrochemical exfoliation of pillared-layer metal–organic framework to boost the oxygen evolution reaction. *Angew. Chem. Int. Ed.* **57**, 4632–4636 (2018).
30. Huang, J. et al. Ion-induced delamination of layered bulk metal–organic frameworks into ultrathin nanosheets for boosting the oxygen evolution reaction. *ACS Sustain. Chem. Eng.* **8**, 10554–10563 (2020).
31. Li, Y. et al. Multistep evolution from a metal-organic framework to ultrathin nanosheets. *Sci. Bull.* **64**, 964–967 (2019).
32. Gajhede, M., Schuller, D. J., Henriksen, A., Smith, A. T. & Poulos, T. L. Crystal structure of horseradish peroxidase C at 2.15 Å resolution. *Nature Struct. Biol.* **4**, 1032–1038 (1997).
33. Almáši, M., Zeleňák, V., Opanasenko, M. & Čejka, J. A novel nickel metal-organic framework with fluorite-like structure: gas adsorption properties and catalytic activity in knoevenagel condensation. *Dalton Trans.* **43**, 3730–3738 (2014).
34. Riou-cavellec, M., Lesaint, C., Nogue, M., Grene, J. & Cedex, L. M. Synthesis, structure, and Mössbauer study of $[Fe(H_2O)_2(C_9O_6H_4)]\cdot H_2O$: a two-dimensional Iron (II) trimellitate (MIL-67). *Inorg. Chem.* **42**, 5669–5674 (2003).
35. Benzaqui, M. et al. A robust eco-compatible microporous iron coordination polymer for CO_2 capture. *J. Mater. Chem. A* **10**, 8535–8545 (2022).
36. Sing, K. S. W. Reporting physisorption data for gas/solid systems with special reference to the determination of surface area and porosity (Provisional). *Pure Appl. Chem.* **54**, 2201–2218 (1982).
37. Groen, J. C., Peffer, L. A. A. & Pérez-Ramírez, J. Pore size determination in modified micro- and mesoporous materials. Pitfalls and limitations in gas adsorption data analysis. *Microporous Mesoporour Mater.* **60**, 1–17 (2003).
38. Chang, C. C., Leeb, J. F. & Cheng, S. Highly catalytically active micro/meso-porous Ti-MCM-36 prepared by a grafting method. *J. Mater. Chem. A* **5**, 15676–15687 (2017).
39. An, Y. et al. The stability of MOFs in aqueous solutions—research progress and prospects. *Green Chem. Eng.* **5**, 187–204 (2024).
40. Wang, C. & Liao, K. Recent advances in emerging metal—and covalent−organic frameworks for enzyme encapsulation. *ACS Appl. Mater. Interfaces* **13**, 56752–56776 (2021).
41. Wang, X., Lan, P. C. & Ma, S. Metal−organic frameworks for enzyme immobilization: beyond host matrix materials. *ACS Cent. Sci.* **6**, 1497–1506 (2020).
42. Mehta, J., Bhardwaj, N., Bhardwaj, S. K. & Kim, K. Recent advances in enzyme immobilization techniques: metal-organic frameworks as novel substrates. *Coord. Chem. Rev.* **322**, 30–40 (2016).
43. Patra, S. et al. Design of Laccase—metal organic framework-based bioelectrodes for biocatalytic oxygen reduction reaction. *ACS Appl. Mater. Interfaces* **8**, 20012–20022 (2016).
44. Cao, Y. et al. Immobilization of *Bacillus Subtilis* lipase on a Cu-BTC based hierarchically porous metal–organic framework material: a biocatalyst for esterification. *Dalton Trans.* **45**, 6998–7003 (2016).
45. Wang, K. Y. et al. Bioinspired framework catalysts: from enzyme immobilization to biomimetic catalysis. *Chem. Rev.* **123**, 5347–5420 (2022).
46. Pylypchuk, I. V., Daniel, G., Kessler, V. G. & Seisenbaeva, G. A. Removal of diclofenac, paracetamol, and carbamazepine from model aqueous solutions by magnetic sol–gel encapsulated horseradish peroxidase and lignin peroxidase composites. *Nanomaterials* **10**, 282 (2020).
47. Wang, L. et al. HRP@ZIF-8/DNA hybrids: functionality integration of ZIF-8 via biomineralization and surface absorption. *ACS Sustain. Chem. Eng.* **7**, 14611–14620 (2019).
48. Christodoulou, I. et al. Degradation mechanism of porous metal-organic frameworks by in situ atomic force microscopy. *Nanomaterials* **11**, 1–17 (2021).
49. Bůžek, D., Adamec, S., Lang, K. & Demel, J. Metal-organic frameworks vs. buffers: case study of UiO-66 stability. *Inorg. Chem. Front.* **8**, 720–734 (2021).
50. Velásquez-Hernández, M. D. J. et al. Degradation of ZIF-8 in phosphate buffered saline media. *CrystEngComm.* **21**, 4538–4544 (2019).
51. Pylypchuk, I. V., Kessler, V. G. & Seisenbaeva, G. A. Simultaneous removal of acetaminophen, diclofenac, and Cd(II) by trametes versicolor laccase immobilized on Fe_3O_4/SiO_2-DTPA hybrid nanocomposites. *ACS Sustain. Chem. Eng.* **6**, 9979–9989 (2018).
52. Moreira, M. T. et al. Formulation of laccase nanobiocatalysts based on ionic and covalent interactions for the enhanced oxidation of phenolic compounds. *Appl. Sci.* **7**, 851 (2017).
53. Becker, D. et al. Removal of endocrine disrupting chemicals in wastewater by enzymatic treatment with fungal laccases. *Org. Process Res. Dev.* **21**, 480–491 (2017).

54. Taheran, M. et al. Covalent immobilization of laccase onto nanofibrous membrane for degradation of pharmaceutical residues in water. *ACS Sustain. Chem. Eng.* **5**, 10430–10438 (2017).
55. Bilal, M., Asgher, M., Iqbal, M. & Hu, H. Chitosan beads immobilized manganese peroxidase catalytic potential for detoxification and decolorization of textile effluent. *Int. J. Biol. Macromol.* **89**, 181–189 (2016).
56. Zhou, W., Zhang, W. & Cai, Y. Laccase immobilization for water purification: a comprehensive review. *Chem. Eng. J.* **403**, 126272 (2021).
57. Grosu, E. F., Cârjă, G. & Froidevaux, R. Development of horseradish peroxidase/layered double hydroxide hybrid catalysis for phenol degradation. *Res. Chem. Intermed.* **44**, 7731–7752 (2018).
58. Cichocka, M. O., Ångström, J., Wang, B., Zou, X. & Smeets, S. High-throughput continuous rotation electron diffraction data acquisition via software automation. *J. Appl. Crystallogr.* **51**, 1652–1661 (2018).
59. Yang, T., Willhammar, T., Xu, H., Zou, X. & Huang, Z. Single-crystal structure determination of nanosized metal–organic frameworks by three-dimensional electron diffraction. *Nat. Protoc.* **17**, 2389–2413 (2022).
60. Kabsch, W. & XDS *Acta Crystallogr. Sect. D* **66**, 125–132 (2010).
61. Sheldrick, G. M. Integrated space-group and crystal-structure determination. *Acta Crystallogr. Sect. A* **71**, 3–8 (2015).
62. Hübschle, C. B., Sheldrick, G. M. & Dittrich, B. ShelXle: a Qt graphical user interface for SHELXL. *J. Appl. Crystallogr.* **44**, 1281–1284 (2011).

Acknowledgements

The authors would like to thank the Swedish Research Council for Internationalization of Higher Education (STINT) for support to the project MG2019-8464, the National Research Foundation of Korea for the framework of international cooperation program (2020K2A9A2A12000250, FY2020), the Swedish Research Council (2022-02939), Formas (2020-00831), the National Research Foundation of Korea (RS-2024-00335713), and the European Commission and Formas (2020-03188) for funding in the frame of the collaborative international consortium (GreenWaterTech) financed under the 2020 AquaticPollutants Joint call of the AquaticPollutants ERA-NET Cofund (GA N° 869178). This ERA-NET is an integral part of the activities developed by the Water, Oceans and AMR JPIs.

Author contributions

The manuscript was written through contributions of all authors. All authors have given approval to the final version of the manuscript. A. Vardanyan-writing the original draft, experimental work, investigation and methodology G. Zhou-writing the original draft, investigation (namely 3DED study, XRD analysis) N. Kim-experimental work T.M. Budnyak- experimental work and writing the part on nitrogen adsorption/desorption isotherms. Prof. Vadim Kessler-funding acquisition (STINT), investigation (XRD analysis), discussion Prof. I.S. Choi-funding acquisition (NRF-Korea), discussion. Z. Huang—writing the original draft, investigation (namely 3DED study, XRD analysis) G.A. Seisenbaeva-conceptualization, supervision, funding acquisition (Formas), investigation (namely AFM, FTIR, TGA), discussion and writing.

Funding

Open access funding provided by Swedish University of Agricultural Sciences.

Competing interests

The authors declare no competing interests.

Additional information

Supplementary information The online version contains supplementary material available at https://doi.org/10.1038/s43246-024-00624-y.

Correspondence and requests for materials should be addressed to Ani Vardanyan or Gulaim A. Seisenbaeva.

Peer review information *Communications Materials* thanks Gift Mehlana and the other anonymous, reviewer(s) for their contribution to the peer review of this work. Primary Handling Editors: Natalia Shustova and Jet-Sing Lee.